Structural Behaviour of Post-installed Reinforcement Bars in Moment Connections of Wall-slabs

A.Y.F. Lee[1], R.K.L. Su[2] and R.W.K. Chan[1*]

[1]*Department of Civil and Infrastructure Engineering, RMIT University, Australia*

[2]*Department of Civil Engineering, The University of Hong Kong, Hong Kong, China*

*Corresponding author. *Email address*: ricky.chan@rmit.au

Highlights

- Full-scale wall-slab connections with post-installed reinforcements are tested.
- The steel ratios and embedment depths of PIR and wall thicknesses are varied in the testing.
- Crack patterns, failure processes and ultimate loads are presented.
- The designing of PIR based on the STM and bonded anchor design method is proposed and validated.

ABSTRACT

Post-installed reinforcement (PIR) bars helps to facilitate retrofitting works, mitigate misplaced reinforcement problems, as well as support newly casted additions. However, the use of PIR has not been addressed in the major reinforced concrete (RC) design codes worldwide. Recently, the European standards have introduced a beneficial coefficient of moments in EN 1992-4 2018 for concrete fastenings which allows compliant PIR systems to be designed by using the bonded anchor (BA) design method. However, when applying this method to wall-slab connection design, the moment resisting capacity is often limited by the lack of bar spacing and small concrete covers. This means that the method neglects long embedment depths and the connections designed based on this method are prone to brittle failure. In this paper, the strut and tie model (STM), which can better describe PIR with long embedment depths, together with the fundamental reinforced concrete (RC) theory is used to improve the ductility of moment connections with PIR bars. An experimental study is conducted to explore the structural behaviour of applying PIR bars that connect the wall and slab. Validations on the proposed STM and supplement to the BA design methods are made. From the experimental findings, measures are then proposed to enhance the ductility of the moment connections.

Key words:

Anchorage, bonded anchor design method, post-installed reinforcement, strut-and-tie model, moment connections

Abbreviations

D Diagonal compressive strut in relevant zone

F_c Compression of reinforcements in relevant zone

F_s Tension force on reinforcements in relevant zone

S_0 Splitting tensile force of concrete

V_1 Applied load

b Width of sample

c_s Concrete cover to centre of reinforcements

f_{bm} Mean adhesive bond strength

f_{ck} Characteristics of the compressive strength of concrete cylinder

f_{ct} Tensile strength of concrete

f_y Tensile strength of reinforcements at yield

f_{yu} Ultimate tensile strength of reinforcements

f'_{ck} Characteristics of the compressive strength of concrete cube

l_b Effective anchorage length providing tensile force by adhesive and PIR interaction

l_{bn} Installed embedment depth

l_m Minimum embedment depth

y_1 Lever arm of applied load

z Lever arm of reinforcements in relevant zone

z_0 Effective lever arm in node zone based on STM

z_{1r} Effective lever arm at connection based on STM

Ψ_M Beneficial coefficient of moments

α Strut efficiency factor

θ Strut inclination angle

σ_{sp} Maximum splitting stress

ϕ Reinforcement diameter

1. Introduction

One of the most commonly used anchoring applications for retrofitting and new projects in the construction industry are post-installed reinforcement (PIR) bars, which are used as adhesive anchors. Holes are drilled into one side of the interface of existing concrete and the bars are inserted into the drilled holes with adhesive. At a later stage, the bars on the other side of the interface are cast into new concrete. This post-installation technology is based on the mechanical characteristics of the original concrete component that needs to be connected to a new structure. This helps to eliminate the problem of the misplacement of reinforcements and allows existing concrete structures to support newly casted components. PIR bars can be applied in almost any location on concrete for rehabilitation and strengthening projects, such as horizontal, vertical, and overhead applications. The PIR bars might have hooks or heads on cast-in part, but not the post-installed end of the structure as they need to be straight. The bars are high in reliability and bearing capacity, rarely damage the original structure during the installation process, and have strong adaptability and applicability, a short construction period, and low installation costs. On top of it all, a more adhesive material will require a shorter embedment depth depending on the concrete grade which defines the strength of the concrete.

The starter bars of cast-in reinforcement (CIR) that are used to provide connections are designed in accordance with Chapter 25 of the ACI 318 Building Code Requirements for Structural Concrete and Commentary [2] in the US and EN 1992-1 (Eurocode 2: Design of concrete structures - Part 1-1: General rules and rules for buildings) [6] in Europe. However, PIR bars are addressed differently in these major design codes. The equivalent standard of performance for the PIR based on the CIR is using the different qualification procedures for adhesion as provided in the EOTA (EAD 330087 Systems for Post-installed Rebar Connections with Mortar [8]) and ICC-ES (AC308 Test Program for Evaluating Adhesive Anchor Systems for Use in Cracked and Uncracked Concrete [1]) in Europe and the US, respectively. Theoretically, PIR can be designed as bonded anchors or STM. The former are designed by using a conventional method such as end anchoring, i.e., equivalent to cast-in reinforcing (EN 1992-1-1 [6]), or bonded anchoring (EN 1992-4 [7] or Chapter 17 of the ACI 318). The latter can be designed based on the procedure in Kupfer et al. [14] and Muenger et al. [20], Clause 6.5 of EN 1992-1-1, or Chapter 23 of the ACI 318.

The bonded anchor (BA) design method states that the load resistance of the concrete cone is influenced by the area of the cone on the concrete surface and the shape of the anchor. If a slab extends across the entire width of the wall, the surface of the cone will be limited by the edges of the wall and small bar spacing. Hence, the resistance of the cone is reduced, which will result in errors if this limitation is neglected. As for a short embedment depth with an inclination angle that is restricted to 25^{o}, the cone failure will influence the design as indicated in ACI 318. In moment connections, the formation of the concrete cone is prevented by the formation of the compressive strut. In response, a new beneficial coefficient of moments has been introduced in BS EN 1992-4 2018 Eurocode 2 Design of concrete structures. Design of fastenings for use in concrete [7]. If the embedment depth is long, splitting or bond failure of the anchorage will take place instead of the formation of a concrete cone. Practically, the BA design method as per EN 1992-4 or Chapter 17 of ACI 318 limits the embedment depth up to 20 bar diameters. On the other hand, when the embedment depth is sufficient enough to bear a larger load, the strut and tie model (STM) is more effective than the BA design method. In fact, the STM is a useful tool for designing moment connections because the model identifies the load path, maintains equilibrium, and shows areas of stress concentration on the concrete. However, it is not so straightforward to use the STM. The size of the struts and ties and the effective anchorage length for resisting tensile force (different to embedment depth, see Eq. (3)) must be known first prior to carrying out the analysis with the STM. Hence, practitioners derive different results for the same engineering problem. In fact, the design process of the PIR, STM and BA design method cannot be mutually exclusive for moderate embedment depths. This inter-relationship should be therefore explored and adequately addressed.

To date, most of the research work in the literature have focused on applying PIR to connect a column or a wall to the foundation. The depth of the connecting elements is usually similar [14,15,16,20]. It is therefore important to examine structures with different embedment depths of the PIR bars. Special consideration is given to one of the main categories of wall-slab (or beam-column) connections in buildings. Recently, a case study on beam-column, beam-wall and column-foundation connections has shown that the designed embedment depth of the PIR varies and inconsistent when different approaches are used [10]. In terms of beam-column and beam-wall designs, the use of both the STM and the BA design method has provided more realistic and practical results. Hence, these two methods are adopted as the basis of the design formulations in this paper. The focus is on the moment connections of the wall-slab joints which have a similar behaviour as that of the beam-column joints. Experiments

on different configurations of the depth and PIR systems have been carried out. Furthermore, the possible failure modes (including yielding of reinforcements (Y-mode), concrete cone failure (C-mode), combined cone and bond failure (B-mode), crushing of the compressive struts (strut and tie failure; S-mode), and shear failure of the wall elements (H-mode)) have been investigated.

2. Method

The wall-slab (or beam-column) connections at the top floor of a building were investigated, which are subjected to higher closing moments than the intermediate floors and have different structural behaviours in comparison to the opening moments of column-foundation connections. The experimental setup is shown in Fig. 1. To facilitate the application of the load, the sample was rotated anticlockwise with the slab upright and wall mounted horizontally on a testing bay. A reinforcement cage for the wall was fixed and welded to a steel angle which would prevent the crushing and displacement of the concrete edges. The wall element (500 W × 1200 L with varying depths) was cast first. Seven days later, the entire contact surface of the new slab connection system was mechanically roughened based on the intended use in accordance with EC2 General rules and rules for buildings in EN 1992-1 [6] (the minimum requirement is a surface with 3 mm of roughness and about 40 mm of spacing between the PIR bars). The mechanical tool used in the experiment had interface roughness factors c and μ (for determining the capacity of the shear stress, τ_{Rdi}) of 0.45 and 0.7, respectively. Holes were drilled by using rotary-impact drills. The drilled holes were then repeatedly cleaned and dried by flushing the holes with water and then using a wire brush to clean them. This was carried out in accordance with the qualifications stipulated for a system that uses PIR bars in the EOTA EAD 330087 [8] and the installation instructions of the PIR bars provided by the manufacturer, Hilti Corporation [13], as it is important for a good bond between the concrete and adhesive. Structural adhesives are usually either organic or inorganic. The former are available pre-packaged in either glass capsules or as two-component packs that require proportioning and mixing before manual injection. The latter are grouted into holes by using grouting tools [4,23]. In this study, the former is used. A two-component resin was injected into the holes with the piston plugs provided by the manufacturer in order to carry out a void-free installation. The PIR bars were inserted immediately prior to the setting of the adhesive. Shear links T10-175 with four legs were installed to slab in order to increase the shear performance of the structure. Three days later, a slab (500 W × 200 D) of a higher concrete grade was cast. Before the 28-day test was carried out, the sample was hauled to a testing bay with cement grouted under the wall for a close contact and to maintain the slab in a vertical

position. The right side of the wall was restricted from moving in both the horizontal and vertical directions by using end notches and holding down bolts, respectively. The steel angle was fixed onto the end notch. A hydraulic jack, with a lever arm *y*, was used to monotonically apply horizontal load on the slab from left to right at a rate of 0.06 mm/s. Hence, the left side of the sample was allowed to move and even bend upwards during loading. The test continued until the ultimate load was reached and softening of the sample occurred. The deformation was monitored by using linear variable differential transformers (LVDTs), strain gauges and digital image correlation (DIC). DIC was carried out by taking digital images every 6 seconds. A layer of lime plaster was applied to the reinforced concrete surface around the connection and randomly sprayed with black paint to form the speckles.

In total, 6 full sized wall-slab samples connected with PIR bars were tested. Commonly found concrete slabs with thickness of 200 mm and a high steel ratio of 0.9% (3T20 bars placed top and bottom (T&B)) were installed onto walls which ranged from those with a similar thickness of 225 mm to ones with a higher thickness of 350 mm and 500 mm. The maximum embedment depths were used. Hence, three wall slab samples with a thickness/embedment depth of 225/200 (10 ϕ), 350/300 (15 ϕ) and 500/460 (23 ϕ) were casted (where ϕ is the bar diameter). In order to determine the influence of the other longitudinal wall reinforcement, another 500/460 (or 23 ϕ) sample was prepared with a layer of longitudinal reinforcement bars in the middle of the wall. For comprehensive testing, two more 500 mm walls with a shear strengthened slab, steel ratio of 1.3% (4T20 T&B) and commonly used embedment depths of 10 ϕ and 20 ϕ were cast [24]. In order to explore the effects of the other failure modes e.g. shear and bending failures of the wall, the far-face (FF) reinforcements were reduced from the typical size of 4T20 to 4T12 in the least thick wall of 225 mm. Furthermore, the longitudinal reinforcement bar at the near-face (NF) of the 500 mm wall with an embedment depth of 20 ϕ was also reduced to 4T16 to examine reinforcement yielding. A rather low concrete grade (about 30 MPa) for the wall was used to determine the effectiveness of using a strong adhesive agent (about 22 MPa). Details on the test samples and concrete properties are given in **Tables 1** and **2**, respectively. The other materials and test parameters are listed in **Table 3**.

A labelling scheme that uses a 3-field alphanumeric code is used in this study, and the fields are defined in Fig. 2. For example, **500C-3-23** means that the thickness of the wall is **500** mm with a layer of reinforcements in the centre (C) of the wall, along with

the PIR bar (ϕ 20 T&B) number (**3**) and the embedment depth (**23 (ϕ)**). In this case, '**C**' denotes the presence of 4ϕ16 longitudinal reinforcements.

3. Experimental structural behaviour

The experimental plates captured by DIC are shown in Appendix A. The possible crack patterns associated with the different failure modes shown by the testing are illustrated in Fig. 3. The parameters for defining the position and orientation of the first primary crack based on the experimental results are listed in **Table 4**. Before discussing the crack patterns of each sample, it should be noted that apart from the PIR yielding (Y-mode), slab collapse rather than wall collapse is the preferred failure mode for connection designs. However, the opposite is necessary here to explore the structural effect of the PIR on an existing wall structure. In the area in which the PIR is connected to the wall, Y-mode failure of the NF reinforcements at the strut and tie node is possible. If the flexural strength of both the slab and wall is similar, the Y-mode failure of the FF reinforcements may also take place. In Fig. 3, the S-mode could take place for concrete cracking, that is, Crack 1 is found at a depth *t* on the PIR if the anchorage is long enough. Once the strut has collapsed, another stronger strut will carry the load in another compression band. Due to the moment effect, the cracked and collapsed strut will immediately lose its load carrying capacity. The load deflection of the slab will increase again and even increase more than the previous highest localized load deflection as shown in Fig. 4. Apart from that, concrete cone failure may occur. Normally, Crack 2 near the PIR end will form first. If the PIR end is near the FF of the wall, half cone failure is found, i.e., the crack propagates until reaching the FF reinforcements. The formation of Crack 4 is normally restrained by another strut as shown in Fig. 3b. The strength of the reinforcements allows new structural integrity. That is, upon further increase of the load, full cone failure will develop when Crack 3 propagates to the existing Crack 1 or 2 (formed by cracking due to STM failure earlier). With a short embedment depth and further distance away from the FF reinforcements, a typical cone failure will occur with Cracks 2 and 4. Under the moment effect, Crack 4 may propagate at a small horizontal angle or even horizontally in order to avoid both the NF and FF reinforcements.

In the experimental results, particular focus is given to the failure modes with the propagation sequence of the first primary crack and second primary crack (if any) and at the peak load. When all of the samples reached about 80% of the peak load, local softening occurred due to the emergence of the first crack which could be observed with the plotted load-deflection of the slab in Fig. 4. Exceptions are Samples

500C-3-23 and 500-3-23 in which the PIR bars have already yielded before the first crack emerged. For similar wall thicknesses (350-500 mm), the first primary cracks develop at a similar deflection (around 11 mm) regardless of the failure mode and the amount of PIR because there is a similar strut inclination angle and concrete strength. More PIR bars or longer embedment depth resulted in higher structural capacity of the samples. The structural softening due to cone failure is unexpected (Samples 225-3-10 and 500-4-10). However, the ductility of these samples is quite different. The first primary cracks develop due to the S-mode failure in Samples 350-3-15, 500-4-20, 500-3-23 and 500C-3-23. Hence, they show good ductility.

Sample 500-4-20 (slab steel ratio of 1.3%) is the stiffest with the highest load-deflection curve. Samples 500-3-23 and 500C-3-23 (slab steel ratio of 0.9%) are slightly lower in stiffness. In fact, they have very similar behaviours. The layer of reinforcements in the centre have almost no effect except for restricting the inclination angle of the struts θ based on the STM from 53^o to 45^o. In these three samples, the depth of the first primary crack t due to diagonal strut failure (S-mode failure) varies from 9 ϕ to 12 ϕ (Fig. 5). The position and orientation of the crack patterns are listed in **Table 4**. Although Sample 500-4-10 has a thicker wall and one more PIR bar than Sample 350-3-15, it is the weakest and even more brittle due to a short embedment depth of 10 ϕ. On the contrary, more ductility is sustained even after half cone failure at the end of the PIR bar in Sample 350-3-15 which is in proximity to the FF reinforcement. Together with Sample 225-3-10, concrete cone failure is found in these three samples. In fact, the least thick sample, Sample 225-3-10, has extensive minor bending cracks at the FF of the wall well before the propagation of the first primary crack.

After the first primary crack emerged, only Sample 500-4-10 became brittle and soon reached the peak load. The other five samples were still ductile. They experienced redistribution of the internal forces either due to the use of FF reinforcements or new compressive struts in the same area. A second primary crack was found in Sample 500-4-20 under the first primary crack, and a third primary crack developed below them after a few seconds passed by. The crack developed due to the half cone failure. The peak load resulted in full cone failure (by Cracks 1 and 3). Second primary cracks (Crack 2) were found throughout the wall i.e., from the half cone failure of Samples 500-3-23 and 500C-3-23 which have the longest embedment depth and PIR bars near the FF of the wall. At the peak load, the slabs collapsed. In the meantime, Crack 3 in the wall started to propagate towards the left from the tip of Crack 1. Although

Sample 350-3-15 only has an embedment depth of 15 ϕ, its second primary crack and peak load have similar behaviours as the other samples with a longer embedment depth (20 ϕ and 23 ϕ) especially Sample 500-4-20. Lastly, the half cone crack and bending in Sample 225-3-10 continued to widen and increase respectively until the peak load was reached.

4. PIR design procedure

The PIR design took into consideration the process of determining the wall element with the reinforced concrete (RC) theory, STM and BA design method. The adhesive strength was assessed based on the European Technical Assessments (ETAs) in the EOTA EAD 330087 [8] or evaluation service reports (ESRs) in AC 308 [1]. The following design equations are mainly based on European codes although some reference is made to the American codes.

4.1. Design of wall element based on RC theory

As discussed, the bending and shear failure of the wall element should be first validated against the results obtained by using the RC theory (EN 1992-1-1 or ACI 318).

4.2. Design of STM

Furthering Schlaich et al. [21], a detailed STM was proposed in Kupfer et al. [14] and Muenger et al. [20], and validated by Hamad et al. [11]. The STM complies with the RC theory and DIN 1045-1 standard - Plain, reinforced and prestressed concrete structures - Part 1: Design and construction [5] in that the tensile forces cannot be transferred directly to the concrete. Four zones can be observed on the wall-slab moment joint; see Fig. 6a. Zone 1 is the newly cast slab while the other slabs are on an existing wall. The connection of the PIR node is in Zone 0 which is between Zones 2 and 3. When an applied moment M_1 is acting on the slab, STM failure takes place to the depth of the effective lever arm or z_0. This will exert a tensile force F_{s1} on the PIR. In order to hold the PIR in place, a concrete compressive strut D_0 with an inclination angle of θ will have to act on a region of PIR across a length of l_b (effective anchorage length at which adhesive and PIR provide the resisting tensile force) in the right side of Zone 0. On the left side, the reacting struts produce a concrete splitting force S_0 and reinforcement forces F_{s0} and F_{s3}.

Anchorage length check

In considering the moment equilibrium of the PIR in Figs. 6a and 6b, a uniformly distributed load (F_{c0}) from the concrete strut of the wall at a lever arm of z_0 based on the STM resists the applied moment M_1 formed by the force V_1 that is acting at the lever arm of y_1 on the slab. Hence,

$$F_{c0} = M_1/z_{c0} = V_1 . y_1/z_0 \quad (1)$$

Similarly, given the effective lever arm of the slab z_{1r} (= $z_1 \cdot k$), the tensile force from the PIR F_{s1} is obtained from Eq. (2).

$$F_{s1} = V_1 . y_1/z_{1r} \quad (2)$$

where z_1 is the distance between the top and bottom reinforcements of the slab. The closing moment in this case, *k*, is taken as 1.0. With reference to Fig. 6b, the tensile force F_{s1} is created by the mean bond strength f_{bm} of the adhesive system through the effective total contact surface with the PIR (=$l_b \cdot \Sigma u$). Hence, together with the total perimeter of the PIR Σu, the effective anchorage length formed in a portion of PIR is

$$l_b = \frac{F_{s1}}{f_{bm} \cdot \Sigma u} \quad (3)$$

The strength of f_{bm} is justified only when there is sufficiently large enough spacing for the PIR in the considered tests. With closer spacing and/or a small cover, the splitting might become decisive (see [13]) and a reduced value should be used for design purposes.

Wall NF and FF reinforcements check

As mentioned above, the concrete strut force F_{c0} is finally resisted by reinforcement forces F_{s0} and F_{s3} through two different sets of struts and ties on the left side of Zone 0 (Fig. 6b). By using moment equilibrium, $F_{s3} \cdot z - F_{c0} \cdot z_0 = F_{s3} \cdot z - (V_1 \cdot y_1/z_0) \cdot z_0 = 0$ at the junction of the PIR and NF reinforcements. The tensile force in the FF reinforcements becomes

$$F_{s3} = V_1 . y_1/z \quad (4)$$

Given that A_{s3} is the area of the FF reinforcements, the reinforcement stress is $\sigma_{s3} = F_{s3}/A_{s3}$. In fact, this equation is found to be the same as the bending check in the conventional RC design.

The free body diagram of Zones 0 and 2 in Fig. 6b is for a balanced cantilever system. A horizontal force equilibrium is maintained by the NF and FF reinforcements together with the force of the concrete struts i.e., $F_{s0} + F_{s3} + F_{c0} = 0$. Using Eqs. (1) and (4),

$$F_{s0} = V_1 . y_1 . \left(\frac{1}{z_0} - \frac{1}{z}\right) \quad (5)$$

Finally the reinforcement stress σ_{s0} (= F_{s0}/A_{s0}) can be obtained where A_{s0} is the area of the NF reinforcements.

According to Kupfer et al. [14] and Muenger et al. [20], z_0 can be determined with $l_{bn} - c_s - l_b/2$ where c_s is the concrete cover and l_{bn} is the installed embedment depth. The location of the cracking or strut failure (Crack 1) is determined by using $t = c_s + z_0$. These two equations are then rearranged to obtain the minimum embedment depth

$$t = c_s + z_0 \quad (6a)$$

$$l_m = t + l_b/2 \quad (6b)$$

However, if l_{bn} is much longer than l_m, a more realistic z_0 needs to be calculated with the strut inclination angle (i.e., $\tan\theta = z_0/z_{1r}$). Thus

$$z_0 = z_{1r} + \tan\theta \quad (7)$$

where the range of the inclination angle is $30^o < \theta < 63^o$. Hence, the location of l_b can be identified by t at a higher up position.

Splitting tensile stress in discontinuity zone

The horizontal nodal force F_{c0} (which is from the concrete strut) acts on the centre of the effective anchorage length l_b which supports the balanced cantilever system as shown in the free body diagram in Fig. 6b. The maximum splitting moment M_{sp} at z_0 is the moment that results from F_{s0} and $F_{c0,}$ i.e., M_{sp} (= $F_{s0} \cdot (z_0 - l_b/2) + F_{s0}^2/(2\, F_{c0}/l_b)$).

Substituting Eq. (1) into (5), $F_{s0} = F_{c0} \cdot (1 - z_0/z)$. The section modulus W_{sp} (= $b \cdot z^2/2.41$) is determined from the transverse rupture stress in the anchorage [14]. Finally, the splitting stress, σ_{sp} (= M_{sp}/W_{sp}), is obtained by:

$$\sigma_{sp} = F_{c0}.z_0.(1 - z_0/z).(1 - l_b/2z).(b.z^2/2.41) \quad (8)$$

The splitting stress obtained with Eq. (8) is checked against the tensile strength of the concrete f_{ct} which can be experimentally determined or indirectly based on the compressive strength of concrete f_{ck} (= $\alpha_{ct} \cdot 0.7 \cdot 0.3 \cdot f_{ck}^{2/3}/\gamma_c$), with coefficient of long term tensile effect, α_{ct} (= 1.0) and partial safety factor for concrete, γ_c (= 1.5) (5).

Compressive strut force in nodal zone

The compressive strut force D_0 is derived from F_{c0} :

$$D_0 = F_{c0}/\cos\theta \quad (9)$$

The strut width is $l_b \cdot \cos\theta$. Based on Eq. 7.3-82 in the Model Code for Concrete Structure (2010) [19], a strut efficiency factor $\alpha = (0.75 \cdot \eta_{fc})$ must be used with $\eta_{fc} = (30/f_{ck})^{1/3} \leq 1$. This is a hyperbolic rather than a linear reduction as per EN 1992-1-1 ($\alpha = k_2 \cdot v'$ with k_2 = 0.85 and $v' = 1\text{-}f_{ck}/250$)). It is found that the lower limit of the strut efficiency factor is 0.6 for normal strength concrete, which is in agreement with Su and Looi [22]. Hence, the strut capacity is:

$$D_R = \alpha.f_{ck}/\gamma_c.(b.l_b.\cos\theta) \quad (10)$$
$$= 0.75(30/f_{ck})^{1/3}.f_{ck}/\gamma_c.(b.l_b.\cos\theta)$$

4.3. Design of bonded anchors based on Eurocode

Under EN 1992 or the ACI standards, PIR bars can be considered as anchors. They can be designed as the end anchorage or bonded anchor in accordance with Eurocode Part 1 (complying with EOTA EAD 330087 [8] which supersedes EOTA TR 023) or the newly released EN 1992 Part 4 (2018) (complying with EAD 330499 [9]), respectively. Apart from reinforcement failure, there are three possible concrete failure modes, including cone, bond or splitting failure. As splitting failure of concrete is only relevant to the design of thin wall members and/or closely spaced reinforcements, this type of failure is not relevant and will not be discussed here. The

design for PIR as the end anchorage can be carried out based on the design for CIR if the performance of the PIR is equal to that of the CIR in both the bond strength $f_b = \tau_R$, and the corresponding slip *s*. The mean bond strength f_{bm} and *s* of the CIR (with a short bond length ($5\phi \leq l_{bn} \leq 10\phi$) and large cover ($c_d \geq 3\phi$)); for example, about 10 MPa and < 0.1 ϕ, respectively for C20/25 concrete [8,17]. As the provisions required for the end anchorage length are based on various safety margins to satisfy all failure modes, they are contradictory for actual bond strength analyses. Therefore, the end anchorage length is not considered in this study. Only the design procedure for the bonded anchor (developed by Herzog [12] for static loads and Mahrenholtz et al. [15], Mahrenholtz and Eligehausen [16] and Mahrenholtz et al. [17] for both static and cyclic loads) is briefly discussed here.

Concrete cone capacity

The bonded anchor theory for the design of fastenings for use in concrete was comprehensively described by Malle and Eligehausen [18] according to CEN/TS 1992-4 (2009). With the published of EN 1992-4 (2018) [7], this CEN/TS was superseded. Nevertheless, the modified BA design method can be also applicable to PIR. In the design equation, the factor k_c, as given in the corresponding European Technical Product Specification, is empirically determined with respect to cracked (k_{cr} = 7.7) or uncracked ($k_{ucr} = k_{cr}/0.7$ = 11) concrete based on the characteristics of the compressive strength of the concrete cylinder f_{ck}. For the compressive strength of the concrete cube f'_{ck}, k_c is 7.2 and 10.1 for cracked and uncracked concrete, respectively. Based on the load and resistance factor design for concrete structures, the mean value of k_{cm} is obtained with $0.75 \cdot k_c$. The cone capacity $N_{Rk,c}$ is determined with an edge distance coefficient $\Psi_{s,N}$ (= $0.7 + 0.3c/c'_{cr,N} \leq 1.0$), shell spalling coefficient $\Psi_{re,N}$ (= $0.5 + l_{bn}/200 \leq 1.0$), group coefficient for different tension loads $\Psi_{ec,N}$ (=1 if uniform load), a partial safety factor γ_{MC} and actual projected area ratio $A_{c,N}/A^0_{c,N}$:

$$N_{Rk,c} = (k_c . f_{ck}^{0.5} . h_{ef}^{1.5}) . A_{c,N}/A^0_{c,N} . \Psi_{s,N} . \Psi_{re,N} . \Psi_{ec,N} . \Psi_{M,N}/\gamma_{MC} \quad (11)$$

where h_{ef} is the effective embedment depth (which is different to l_b in STM), $A_{c,N}^0 = s_{cr,N}^2 = (3 \cdot h_{ef})^2$, $\gamma_{MC} = \gamma_c \cdot \gamma_{inst}$ and

$$\Psi_{M,N} = 2 - z_1/1.5h_{ef} \quad \text{or} \quad (12a)$$

$$\Psi_M = 2.5 - z_1/h_{ef} \quad (12b)$$

The moment coefficient Ψ_M [12,15,16] given in Eq. (12b) has been recently introduced to reflect the effect of moment induced confinement stress. It is derived from tests and numerical simulations. However, the beneficial compressive effect of the moment may prevent the formation of the cone or even cause bond failure. Eq. (12a) is therefore first adopted from EN 1992-4 (2018) which is somewhat conservative. Although Ψ_M should be larger than 1.0, with the inclination angle of the struts based on the STM in the range of $30^o < \theta < 63^o$, we propose a limitation of $1.1 \geq \Psi_M \geq 2$ for Eq. (12). Moreover, if the cracking propagates at an angle outside this range, Ψ_M is no longer applicable.

The effective embedment depth h_{ef} may be taken as l_{bn} in the STM. However, in the presence of three or four edges with $c_i < c_{cr,N}$ ($= s_{cr,N}/2 = 1.5 \cdot l_{bn}$), h_{ef} should be calculated by using Eq. (13) together with modified characteristic spacing $s'_{cr,N}$ ($= s_{cr,N} \cdot h_{ef}/l_{bn}$) and critical edge distance $c'_{cr,N}$ ($= c_{cr,N} \cdot h_{ef}/l_{bn}$).

$$h_{ef} = \max\left\{l_{bn}\frac{c_{max}}{c_{cr,N}}, l_{bn}\frac{s_{max}}{s_{cr,N}}\right\} \quad (13)$$

Combined cone and bond capacity

The bond strength is assumed to be uniform along the installed embedment depth from 4 ϕ to 20 ϕ. With increased the embedment depth, the failure mode might change from cone to splitting or bond (pullout) failure. Bond failure usually takes place simultaneously with concrete cone failure on the top of the anchorage area. Two combined failure modes, cone failure and bond failure, then develop. However, most of time, it is challenging to differentiate between cone failure and cone and bond failures. Given an adhesive bond strength τ_{Rk} ($= 0.75 \cdot f_{bm}$) based on the European Technical Product Specification and EN 1992-4, the combined capacity $N_{Rk,p}$ is given by Eq. (14a):

$$N_{Rk,p} = (\tau_{Rk}.\pi.\phi.h_{ef}).A_{p,N}/A^0_{p,N}.\Psi_{g,Np}.\Psi_{s,Np}.\Psi_{re,N}.\Psi_{ec,Np}/\gamma_{Mp} \quad (14a)$$

$$N_{Rk,p} = (\tau_{Rk}.\pi.\phi.h_{ef}).A_{p,N}/A^0_{p,N}.\Psi_{g,Np}.\Psi_{s,Np}.\Psi_{re,N}.\Psi_{ec,Np}.\Psi_{M,N}/\gamma_{Mp} \quad (14b)$$

where $\gamma_{Mp} = \gamma_{MC}$, $s'_{cr,Np} = 7.3\ \phi \cdot \tau_{Rk}^{0.5} \leq 3 \cdot h_{ef}$, $\Psi_{g,Np}$ is the group effect, the edge distance coefficient $\Psi_{s,Np} = 0.7 + 0.3c/c'_{cr,Np} \leq 1.0$, $\Psi_{ec,Np} = 1$ for uniform load and the actual projected area $A_{p,N}^0 = c'^2_{cr,Np} = s'^2_{cr,Np}/4$. It is noted that the beneficial coefficient of the moments $\Psi_{M,N}$ is not included in EN 1992-4 Eq. (14a). However, if $30^o < \theta < 63^o$ in the moment connection design, we recommend the use of Eq. (14b)

to reflect the increase in the bond strength by the compressive stresses that are acting at the lower end of the anchorage.

5. Predicted results vs. experimental results

In order to compare the theoretical results with the experimental results, all factors of safety for loads and materials are excluded in this discussion. Moreover, the mean bond strength of the adhesive agent provided by the manufacturer f_{bm} = 21.6 MPa can better explain the structural behaviour of PIR than the design bond strength of 11.6 MPa (by using the equations in [3,8,13]) even for a low concrete grade of 30 MPa. In fact, a high bond strength of up to 36 MPa can be used with a low concrete grade of 20 MPa, as in [15]. The theoretical results (V_{theo}) obtained from the equations discussed in the previous section are presented in **Table 6**. These have been validated against the experimental results (V_{exp}) to confirm the validity of the equations and identify the observed failure modes.

5.1 RC design theory

The theoretical behaviour to be discussed is mainly based on the STM and the BA design method. However, based on the experimental results, it is not surprising that the conventional RC design theory needs to be validated first. At the first primary crack load of 39 kN, Sample 225-3-20 undergoes bending failure at the FF of the wall reinforcements. Both the RC design theory and STM (Eq. (4)) provide the same load value of 38 kN (**Table 6**). In addition, the wall shear load to capacity ratio of 0.98 was obtained with Sample 500-4-20 under the peak load. Hence, both bending and shear checks must be conducted as part of the design.

5.2 STM

The tensile forces in the PIR F_{s1} were recorded by the strain gauges installed on the PIR. **Table 5** shows the experimental and theoretical tensile strengths of the PIR. As expected, the theoretical loads V_{theo} somewhat reduce the yield strength of the PIR in comparison to the experimental loads V_{exp}. The experimental tensile tests of the PIR show that the ultimate strength is 1.15 of the yield strength. Hence, upon reaching the yield strength, the applied load could still be increased to the same extent. The F_{s1} are used to determine the effective lever arm of the slab z_{1r} from the applied moment M_1 (Eq. (2)). In Fig. 7, when the PIR yields, the z_{1r} is found to be very close to z_1 (=130 mm) which concurs to the assumption that $z_{1r} = z_1$ for closing moment connections [14]. The inclination angle θ is also important for calculating the effective strut depth

z_0. Theoretically, the lower limit is 30^o. However, the use of the STM with an overly small or large θ will be ineffective. In practice, slabs are normally thinner than walls. As a result, the θ is normally larger than 45^o. **Table 4** shows the θ based on the STM which ranges from 45^o to 54^o. Due to the presence of a layer of reinforcements in the centre of Sample 500C-3-23, a crack formed at 45^o. If the experimental θ is used to determine z_0 (Eq. (7)), the position of the strut crack (Crack 1) *t* may be obtained. This semi-analytical calculation agrees well with the experimental result (Fig. 5). As discussed above, it is not a straightforward task to determine the effective anchorage length by choosing a suitable θ. However, once the effective anchorage length has been determined, the location of the first primary crack can be accurately predicted (**Table 4**). Otherwise, if the STM is based on a long end embedment depth, the result will be unacceptable as per Kupfer et al. [14] and Muenger et al. [20]. Hence, the direct use of the lower bound of the strut capacity of $\theta = 60^o$ for determining the z_0 is suggested here for simplicity.

Using the equation for FF wall reinforcements based on the STM, the weakest reinforcement (4T12) that was installed in Sample 225-3-10 experienced yielding failure. In terms of the NF wall reinforcements which had the lowest strength, 4T16 which was installed in Sample 500-4-20, also experienced yielding at around the peak load. With an anchorage length of 15 ϕ or longer, the first primary crack initiated in Samples 350-3-15, 500C-3-23, 500-3-23 and 500-4-20 when approaching the strut capacity. The broken strut was immediately replaced by using a nearby strut. This process was repeated until the ultimate yield of the PIR took place at a higher capacity based on the STM. The peak loads of the four samples then occurred and listed in **Table 6**. In general, the splitting tensile force in concrete is inhibited by the bending of the wall structure for cases with closing moments. Splitting failure is not controlled. If the location of the crack *t* is added to half of the effective anchorage length, the minimum required embedment depth (l_m), as listed in **Table 4**, is obtained by using Eq. (6). Fig. 8 shows the theoretical peak loads (V_1) and the corresponding embedment depths based on an assumed θ of 60^o. As l_m is a function of c_s, θ, z_{1r} and V_1, l_m will be very similar in each case if V_1 is varied slightly and the others are kept constant. The PIR system with $l_m \approx 15$ ϕ is found to be effective in forming the STM regardless of the wall thickness. The simplified theoretical results based on the STM are provided in **Table 7**.

5.3 Bonded anchor theory

It is difficult to identify cone and bond failures through experiments. In cases that involve high bond strength (due to the use of high strength adhesive agents), cone failure usually occurs as opposed to bond failure. Sample 500-4-20 shows that if the failure load of the cone and strut is similar, cracking due to the latter will occur first at the upper part of the PIR due to the shorter load path (i.e. Crack 1 rather than Crack 2 is found). In an effective strut and tie system, the compressive strut will cause cone failure due to cracking to a higher location which is usually found at the first primary crack rather than the tip of the PIR as shown in Fig. 3b (i.e. Crack 3 rather than Crack 4 is found). By introducing a beneficial coefficient of the moments Ψ_M (Eq. (12)) in the inclination angle which ranges $30^o < \theta < 63^o$, the theoretical results based on the BA design method are consistent with the experimental results (Fig. 9 and **Table 6**). Samples 250-3-10 and 500-4-10 with a minimum embedment depth (l_m) of 10 ϕ have an inclination angle of 57^o. Ψ_M can be used to determine the cone failure more accurately, which is especially the case for Sample 250-3-10, which validates the presence of B-mode failure. For marginal cases, such as Sample 350-3-15 (15 ϕ) with $\theta = 66^o > 63^o$, Ψ_M would help to determine exactly the point of full cone failure (Cracks 1 and 3) at a peak load 80 kN. For the theoretical first primary crack load, an adjustment (= $\tan 63^o/66^o$) to 80 kN would give 66 kN which is very close to the experimental load of 62 kN. On the other hand, Ψ_M obviously should not be used for half cone failure (Crack 2) as in Sample 500-4-20 (20 ϕ) with $\theta = 88^o$. The half cone failure causes the emergence of the second primary crack. The theoretical and experimental loads are 111 kN and 110 kN, respectively. For the rest of the samples, that is, Samples 500-3-23 and 500C-3-23 with $l_m > 20$ ϕ, the BA design method is no longer accurate or even inapplicable as shown in Fig. 9.

5.4 Combined theoretical design equations

Combining theoretical design equations could verify and explain for the observed test results (Appendix A). A better understanding of the structural behaviour of each PIR sample can then be obtained. Detailed comparisons are provided in **Table 6**.

Sample 250-3-10

At a load of 27 kN, bending cracks starts to propagate at the FF of the wall near the notch support. At a load of 39 kN, the first primary crack emerges (Crack 2) due to failure of the C and Y modes (half cone failure and yielding of FF reinforcements). At a peak load of 45 kN, the FF reinforcements reach their ultimate strength. A bending crack propagates almost all the way across the wall section (Crack 5). The amount of B-mode failure is then estimated.

Sample 500-4-10

The first primary crack emerges at the ends of the PIR due to the initiation of C-mode failure (Crack 2) at a load of 59 kN. Full cone failure develops due to the short embedment depth and further distance from the FF of the wall, (Cracks 2 and 4) at a peak load of 74 kN. Crack 2 propagates horizontally due to the bending effect. A peak load of 84 kN due to the yield of the edge reinforcements is observed.

Sample 350-3-15

The first primary crack emerges due to the C-mode of failure (Crack 2) at a load of 63 kN. The Y-mode of failure at the PIR takes place at a load of 70 kN. As the FF reinforcements inhibit half cone failure, the structure is thereby stabilized until ultimate yield of the PIR. The second primary crack emerges at a load of 77 kN due to the failure of the strut and tie, or the S-mode. At the peak load of 80 kN, full cone failure (C-mode) develops (Cracks 1 and 3 emerge) with an increase of the Ψ_M.

Sample 500-4-20

The first primary crack (Crack 1) develops due to S-mode failure at a load of 93 kN. Y-mode failure at the PIR is recorded at a load of 98 kN. The second primary crack develops at a load of about 110 kN. This is another form of S-mode failure caused by the reaching of the ultimate yield of PIR. At the peak load of 127 kN, the full cone failure (Cracks 1 and 3), yield of the NF reinforcements and wall shear failure are estimated.

Sample 500-3-23

The Y-mode failure at the PIR and the development of first primary crack (Crack 1) due to S-mode failure are recorded at loads of 83 kN and 91 kN respectively. The second primary crack is found below the first primary crack and propagates towards the FF reinforcements probably due to the C-mode failure (Crack 2) at a load of 95 kN. At the peak load of 100 kN, micro cracks (Crack 3) initiate at the tip of Crack 1 in the horizontal direction. This is another form of S-mode failure caused by the reaching of the ultimate yield of PIR. At the same time, the slab is damaged.

Sample 500C-3-23

Sample 500C-3-23 is very similar to Sample 500-3-23 except for a smaller strut angle due to a layer of reinforcements in the centre. Y-mode failure at the PIR is found at a load of 78 kN. The first primary crack develops due to S-mode failure at a load of 89 kN. The second primary crack propagates below the first primary crack toward the FF reinforcements (Crack 2) at a load of 102 kN which is also the peak load. Micro cracks in the horizontal direction that join Cracks 1 and 3 develop immediately. This is another S-mode failure caused by the reaching of the ultimate yield of PIR. The slab is heavily damaged.

6. Conclusion

Six wall-slab samples with PIR bars of various steel ratios, embedment depths and wall thicknesses are tested to investigate the effect of the structural behaviour on the crack patterns and failure modes. A high adhesive bond strength of 21.6 MPa based on an investigation is found to be effective even in structures with a low concrete grade of 30 MPa. Based on the experimental results, methods for standardizing the design procedure and predicting the crack patterns are proposed. The traditional RC theory for bending and shear checks must be validated prior to conducting analyses with the STM and the BA design method. After some modifications are proposed, the STM and BA design method can both satisfactorily describe failure behaviour. The use of the BA design method or STM depends on the installed embedment depth, in which $l_{bn} \leq 15\ \phi$ or $l_{bn} \geq 15\ \phi$, respectively. At $l_{bn} = 15\ \phi$, strut and tie cracks start to develop before cone cracks emerge. However, when $15\ \phi \leq l_m \leq 20\ \phi$, both methods are necessary for better prediction of the crack patterns and failure modes. A theoretical calculation example is given in Appendix B. In practice, slabs damage and yield of the PIR are preferred rather than damage and yield of the walls and other structural elements. However, as shown in the experiments, the yield (even the ultimate yield) of the PIR may initiate damage to the slabs and/or walls. In order to avoid sudden collapses due to cone failure, the ductility of the slabs and/or walls can be increased by anchoring PIR in the proximity of FF reinforcements. Alternatively, a sufficient embedment depth ($\geq 15\ \phi$) should be in place for the effectiveness of the STM.

The equations based on the STM presented in this paper basically follow those in Kupfer et al. [14] and Muenger et al. [20]. However, some modifications are made and observations provided. The sequence of analysis includes checking the NF and FF reinforcements as they may yield before compressive strut failure which is neglected in the BA design method. The presence of other intermediate or longitudinal wall reinforcements in the centre of the slab will not affect the behaviour too much aside from the strut inclination angle. The position of strut failure (first primary crack) t and the minimum embedment depth l_m are found to be reliable. A simpler but lower bound equation based on the STM is suggested for standardizing $\theta = 60^o$ and proven effective at an embedment depth of about $15\ \phi$. Hence, for closing moment cases, l_m and z_0 are obtained from Eqs. (6) and (7), respectively. In checking the compressive strut capacity, the strut efficiency factor α is calculated with hyperbolic rather than linear reduction.

For the BA design method, EN 1992-4 2018 has provided a new beneficial coefficient of moments Ψ_M to account for the strut strengthening effect on cone failure. From the experiments, it is recommended that Ψ_M does not exceed the value of 2.0 with a strut angle that ranges $30^o < \theta < 63^o$, and should not be used with cones with an inclination angle that is larger than 63^o. Hence for PIR bars with a long embedment depth, cone failure will not develop in the region with Ψ_M but at the tips of the PIR without Ψ_M. Although the code does not specify the use of Ψ_M for bond failure or combined cone and bond failure, its application is recommended in this paper.

The inter-relationship between the STM and the BA design method for the moment connections of wall-slabs with PIR has been established on the transmission and distribution of forces, and development and propagation of cracking. Engineers and practitioners could adapt the proposed standardized design procedure and design based on the crack patterns, ductility and available embedment depth and adhesive material. However, for cases with large moment connections, a long embedment depth based on the STM is the only viable method. More research could be done to investigate the effect of adhesive systems on cracking in resisting different moment connections with PIR. The structural difference between PIR and CIR in this type of wall-slab connection can be explored further in order to promote the use of PIR as an economical and sustainable means of reinforcements.

7. Acknowledgement

The authors would like to thank the financial support of the RGC Research Impact Fund (R7027-18) entitled “Modular Integrated Construction 2.0+” for Quality and Efficient Tall Residential Buildings through Advanced Structural Engineering, Innovative Building Materials and Smart Project Delivery, the technical support of Hilti (Hong Kong) Ltd. and the assistance of Mr. Yanlong Zhang for carrying out some of the tests.

References

[1] AC 308 (2016) Post-installed Adhesive Anchors in Concrete Elements. Whittier, California: *International Code Council Evaluation Service, Inc*. (ICC-ES).

[2] ACI committee 318 (2014) Building code requirements for structural concrete: *(ACI 318-14)* and commentary *(ACI 318R-14)*. Farmington Hills, Michigan: American Concrete Institute.

[3] Charney F. A., Pal K., Silva J. (2013) Recommended Procedures for Development and Splicing of Post-Installed Bonded Reinforcing Bars in Concrete Structures. *ACI Structural Journal,* **110**(3), pp. 437.

[4] Contrafatto, L. and Cosenza, R. (2014) Behaviour of post-installed adhesive anchors in natural stone. *Construction and Building Materials*, **68**, pp. 355-369.

[5] DIN 1045-1 (2017) Plain, reinforced and pre-stressed concrete structures Part 1. Design and construction.

[6] EN 1992-1-1 (2004) Eurocode 2 Design of concrete structures Part 1-1: General rules and rules for buildings. *European Committee for Standardization (CEN).*

[7] EN 1992-4 (2018) Eurocode 2 Design of concrete structures Part 4: Design of fastenings for use in concrete, *European Committee for Standardization (CEN).*

[8] EOTA EAD 330087 (2018) Systems for Post-installed Rebar Connections with Mortar, *European Organisation for Technical Assessment*.

[9] EOTA EAD 330499 (2017) Bonded Fasteners for Use in Concrete, *European Organisation for Technical Assessment*.

[10] Genesio, G., Nerbano, S., Piccinin, R. (2017) Design of moment resisting reinforced concrete connections using post-installed reinforcing bars. *3rd International Symposium on Connections between Steel and Concrete, Stuttgart, Germany*.

[11] Hamad, B. S., Al Hammoud, R., Kunz, J. (2006) Evaluation of Bond Strength of Bonded-In or Post-Installed Reinforcement. *ACI Structural Journal, 103(2), pp. 207.*

[12] Herzog, M. (2014) Unification of the design concept for reinforced concrete and concrete anchors. *Dissertation, University of Stuttgart.*

[13] Hilti Corp. (2016) Post-installed reinforcing bar guide. *Hilti documentation*.

[14] Kupfer, H., Münger, F., Kunz, J., Jähring, A. (2003) Bonded-in reinforcement for frame node connections. *Bauingenieur*, **78**, pp.24-38.

[15] Mahrenholtz, C., Akguzel, U., Eligehausen, R. and Pampanin, S. (2014) New Design Methodology for Seismic Column-to-Foundation Anchorage Connections. *ACI Structural Journal,* **111**(5), pp. 1179.

[16] Mahrenholtz, C. and Eligehausen, R. (2016) Simulation of Tests on Cast-In and Post-installed Column-to-Foundation Connections to Quantify the Effect of Cyclic Loading. *Journal of Structural Engineering,* **142**(1), pp. 04015073.

[17] Mahrenholtz, C., Eligehausen, R. and Reinhardt, H. (2015) Design of post-installed reinforcing bars as end anchorage or as bonded anchor. *Engineering Structures,* **100**, pp. 645.

[18] Malle, R. and Eligehausen, R. (2013) Design of Fastenings for Use in Concrete. *DE: John Wiley & Sons Inc*.

[19] Model Code for Concrete Structures (2010) International Federation for Structural Concrete (fib).

[20] Muenger, F., Kupfer, H, Jaehring, A., Kunz, J. (2002) Boned-in reinforcement for frame node connections. *Bond in Concrete-from research to standards*, pp. 1-8.

[21] Schlaich J, Schäfer K, Jennewein M., Silva J. (1987) Toward a Consistent Design of Structural Concrete. *PCI Journal, 32(3),* pp. 74-150.

[22] Su, R.K.L. and Looi, D.T.W. (2016) Revisiting unreinforced strut efficiency factor. ACI *Structural Journal*, **113** (2), pp.301-302.

[23] Wang, D., Wu, D., He, S., Zhou, J. and Ouyang, C. (2015) Behavior of post-installed large-diameter anchors in concrete foundations. *Construction and Building Materials,* **95**, pp. 124-132.

[24] Xie, Q., Xue, S., Xu, X. (2018) Study on seismic damage model of post-installed connection between steel and concrete. *Int J Civ Eng*, **15**, pp.1201-1211.

Table 1 Details of test samples

Sample	**225-3-10**	**350-3-15**	**500-4-10**	**500-3-23**	**500C-3-23**	**500-4-20**
Wall thickness (mm)	225	350	500	500	500	500
PIR	3ϕ20T&B	3ϕ20T&B	4ϕ20T&B	3ϕ20T&B	3ϕ20T&B	4ϕ20T&B
Anchorage (mm)	200 (10ϕ)	300 (15ϕ)	200 (10ϕ)	460 (23ϕ)	460 (23ϕ)	400 (20ϕ)
Lever arm, y (mm)	1160	1035	885	885	885	885
Wall reinforcements	4ϕ20NF 4ϕ12FF	4ϕ20EF	4ϕ20EF	4ϕ20EF	4ϕ20EF	4ϕ16NF 4ϕ20FF

Table 2 Concrete properties at 28 days

Sample	**225- 3-10**	**350- 15-3**	**500- 4-10**	**500- 3-23**	**500C-3-23**	**500- 4-20**
Cube strength of slab f'_c (MPa)	40.7	42.0	46.8	38.8	47.3	43.5
Tensile strength of wall f_{ct} (MPa)	2.69	2.32	2.03	2.54	2.53	2.49
Cube strength of wall f'_c (MPa)	34.6	32.5	33.5	32.6	32.2	35.3
Young's modulus of wall (GPa)	23.9	23.1	20.3	21.1	21.5	24.4

Table 3 Material and setup parameters

Adhesive bond strength	**Reinforcements**					**Concrete cover to centre of reinforcements**		
f_{bm} (MPa)	f_y (MPa)	f_{yu} (MPa)	E (GPa)	wall z (mm)	slab z_1 (mm)	wall c_s (mm)	Slab (mm)	PIR c_{max} (mm)
21.6	540	621	196	410	130	45	35	82.5

Table 4 Patterns of first primary crack

STM	**500-3-23**				**500C-3-23**				**500-4-20**			
	V	θ°	t	l_m	V	θ°	t	l_m	V	θ°	t	l_m
Test	91	53	244	460	89	45	187	460	93	50	200	400
Semi analytical	89	53*	173	295	87	45*	175	238	96	50*	200	260
Lower bound	79	60	270	333	78	60	270	333	85	60	270	323
Kupfer [14]	57	71	412	460	56	71	413	460	70	67	356	400
STM	**225-3-10**				**350-3-15**				**500-4-10**			
	V	θ°	t	l_m	V	θ°	t	l_m	V	θ°	t	l_m
Test	45	44	170	200	77	54	239	300	74	43	167-	200
Lower bound	63	60	270	339	67	60	270	335	80	60	270	320
Kupfer [14]	66	33	129	200	72	55	230	300	90	37	144	200

Note: V – peak load (kN); t – depth (mm) of compressive strut crack (see Fig. 3a.); l_m– minimum embedment depth of PIR (mm); θ – compressive strut angle; *– from test angle and z_{1r}

Table 5 Experimental and theoretical tensile strengths of PIR

	225-3-10	500-4-10	350-3-15	500-4-20	500-3-23	500C-3-23
PIR failure mode	-	-	Y	Y	Y	Y
V_{exp} (kN)	NA	NA	70	98	83	78
V_{theo} (kN)	57	79	64	100	75	75
V_{exp}/V_{theo}	NA	NA	1.09	0.98	1.11	1.04

Note: Y – yield; V_{exp} – experimental load at yield; and V_{theo} – theoretical load.

Table 6 Experimental and theoretical results

	225-3-10	500-4-10	350-3-15	500-4-20	500-3-23	500C-3-23
At 1st primary crack formed						
Possible failure mode	Y^u,C	C	C,S	S	Y,S	Y,S
1st prim. crack load V_{exp}	39 kN	59 kN	63 kN	93 kN	91 kN	89 kN
Cone V_{theo}	37 kN	75 kN	66 kN	-	-	-
Cone V_{exp}/V_{theo}	1.05	0.79	0.95	-	-	-
STM failure V_{theo}	72 kN	92 kN	71 kN	96 kN	87 kN	89 kN
STM failure V_{exp}/V_{theo}	0.54	0.64	0.89	0.97	1.04	1.00
NF reinforcements R	0.04	0.45	0.37	0.76	0.40	0.62
FF reinforcements R	1.15	0.19	0.37	0.30	0.29	0.29
At 2nd primary crack formed						
Possible failure mode	-	-	C,S	C,Y,S	Y^u,C	Y^u,C
2nd prim. crack load V_{exp}	-	-	77 kN	110 kN	95 kN	102 kN
Cone V_{theo}	-	-	80 kN	118 kN	81 kN	80 kN
STM failure V_{theo}	-	-	82 kN	111 kN	-	-
At peak load						
Possible failure mode	Y^F,C	C	Y^u,C,S	S,C,Y^u, Y^N,H	Y^u,S	Y^u,S
Peak load V_{exp}	45 kN	74 kN	80 kN	127 kN	100 kN	102 kN
Cone V_{theo}	45 kN	75 kN	80 kN	237 kN	160 kN	159 kN
Cone V_{exp}/V_{theo}	1.00	1.00	0.96	0.48	0.62	0.64
STM failure V_{theo}	72 kN	105 kN	83 kN	111 kN	100 kN	102 kN
STM failure V_{exp}/V_{theo}	0.62	0.70	0.96	1.14	1.0	1.0
Shear R	0.74	0.58	0.73	0.98	0.78	0.79
NF reinforcements R	0.04	0.53	0.17	1.0	0.38	0.61
FF reinforcements R	1.15	0.21	0.40	0.40	0.28	0.28

Note: Y – PIR yield, Y^u – PIR ultimate yield, Y^N – NF reinf. yield, Y^F – FF reinf. yield, C – cone, B – combined cone & bond, S – strut, H – shear; underline refers to possible failure; V_{exp} – experimental peak load; V_{theo} – theoretical peak load; R – relevant failure mode capacity ratio when subjected to applied peak load V_{exp} and failed approximate to 1.0.

Table 7 Simplified theoretical results with $\theta = 60^o$ based on STM

V_{exp}/V_{theo}	225-3-10	500-4-10	350-3-15	500-4-20	500-3-23	500C-3-23
1st maj crack load V_{exp}	39 kN	59 kN	63 kN	93 kN	91 kN	89 kN
V_{exp}/V_{theo}	0.62	0.74	0.94	1.09	1.15	1.14
Peak V_{exp}	45 kN	74 kN	80 kN	127 kN	100 kN	102 kN
V_{exp}/V_{theo}	0.62	0.79	1.11	1.29	1.11	1.14

Note: V_{exp} – experimental load; V_{theo} – theoretical load.

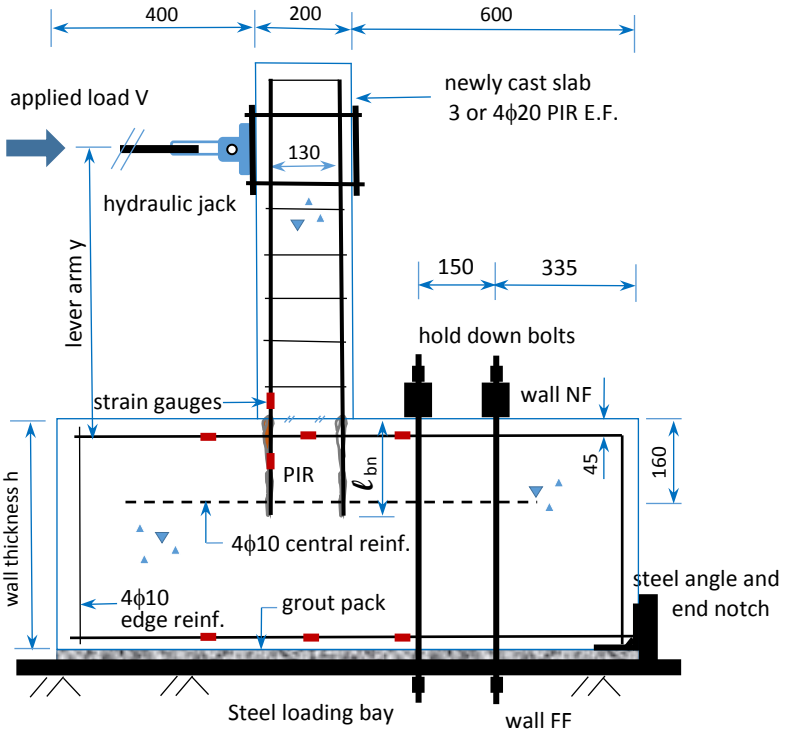

Fig. 1. Experimental setup

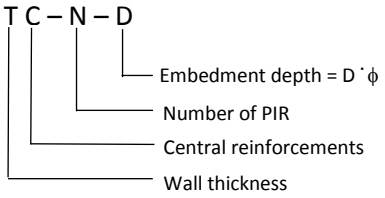

Fig. 2. Labelling of test samples

Note: all in mm; ϕ is reinforcement diameter

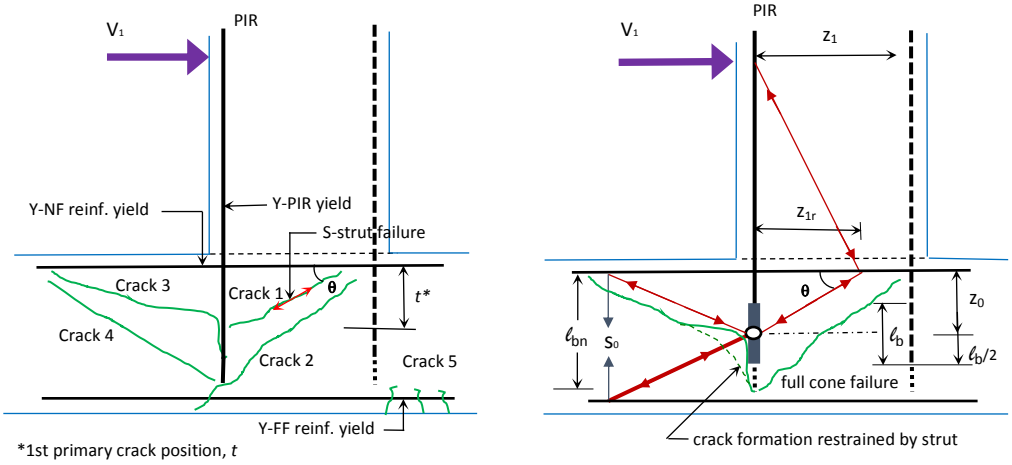

Fig. 3. Crack patterns (a) major possible failure modes and (b) restrained cone failure

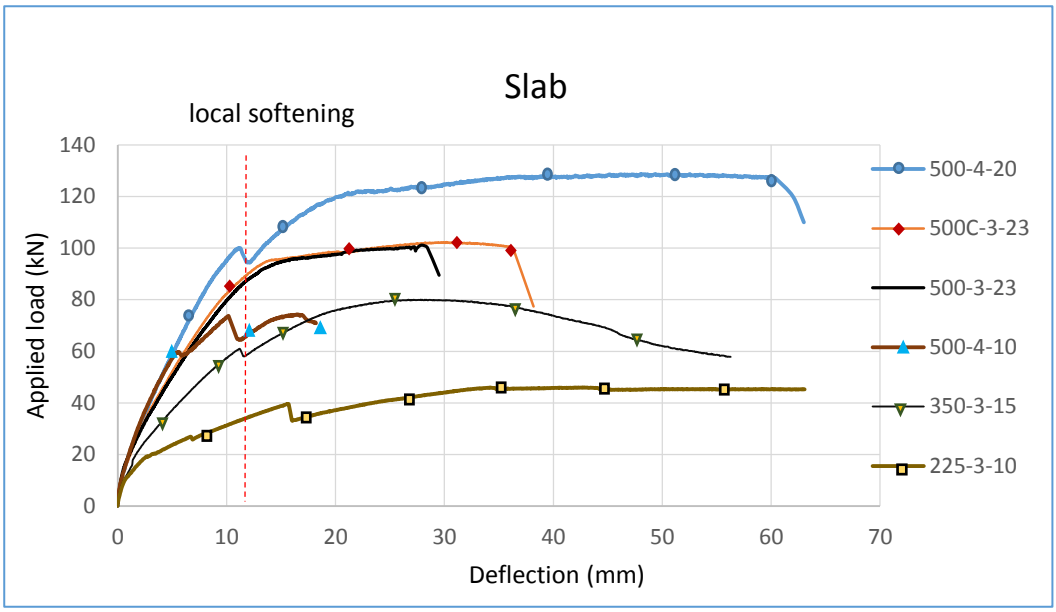

Fig. 4. Plotted load-deflection

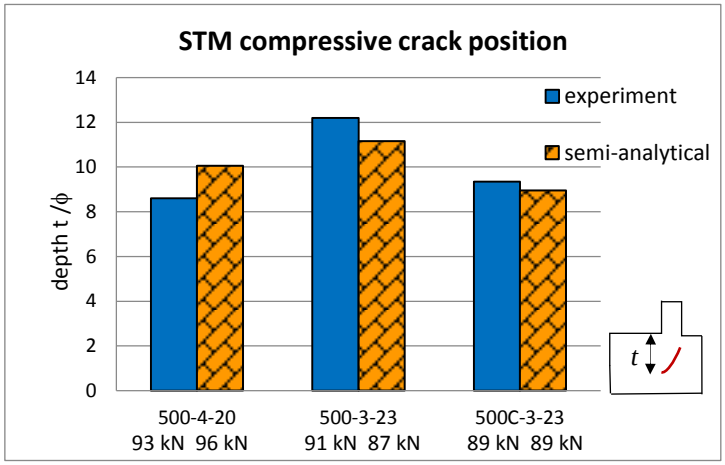

Fig. 5. 1st primary crack position – STM failure

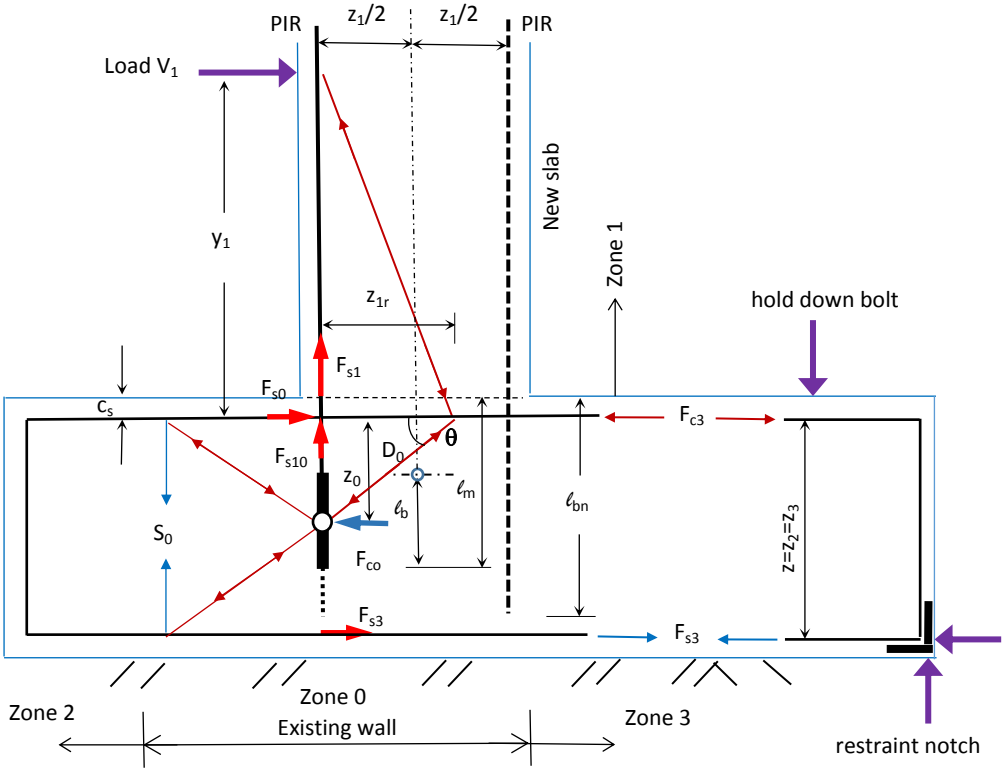

Fig. 6a. Load path based on STM failure

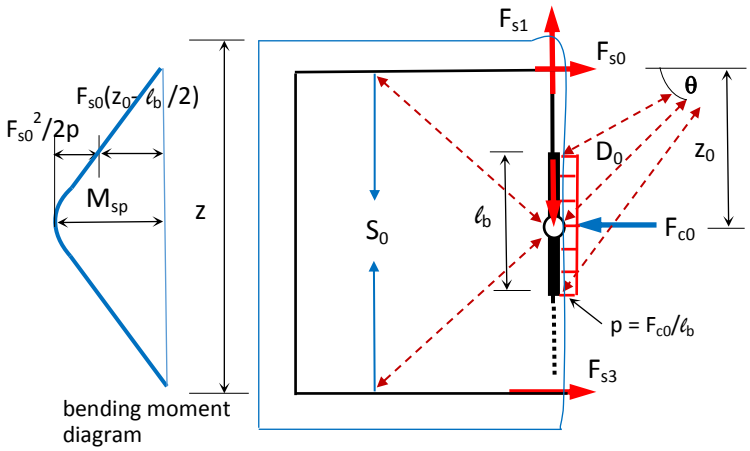

Fig. 6b. Free body diagram for determining splitting moment S_0

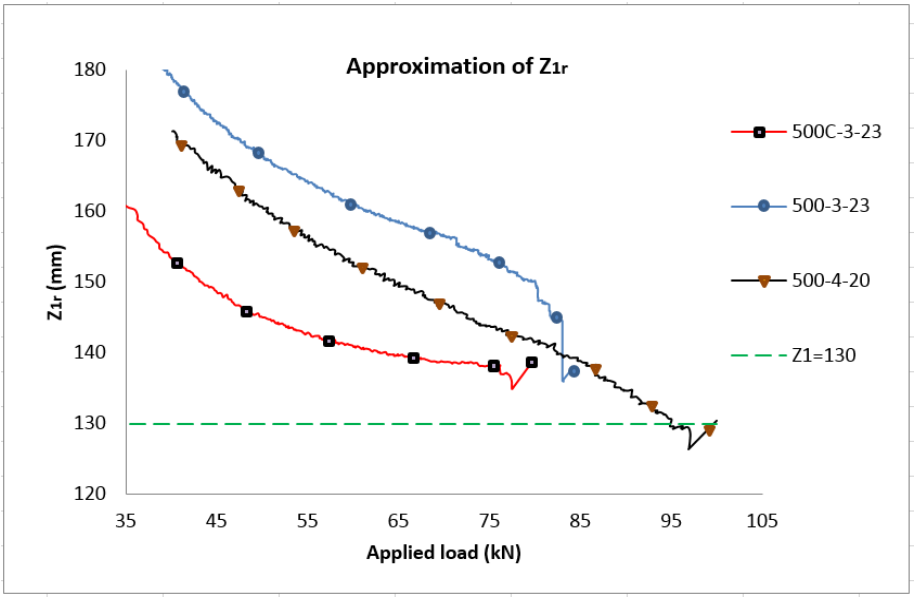

Fig. 7. Determining effective lever arm of slab

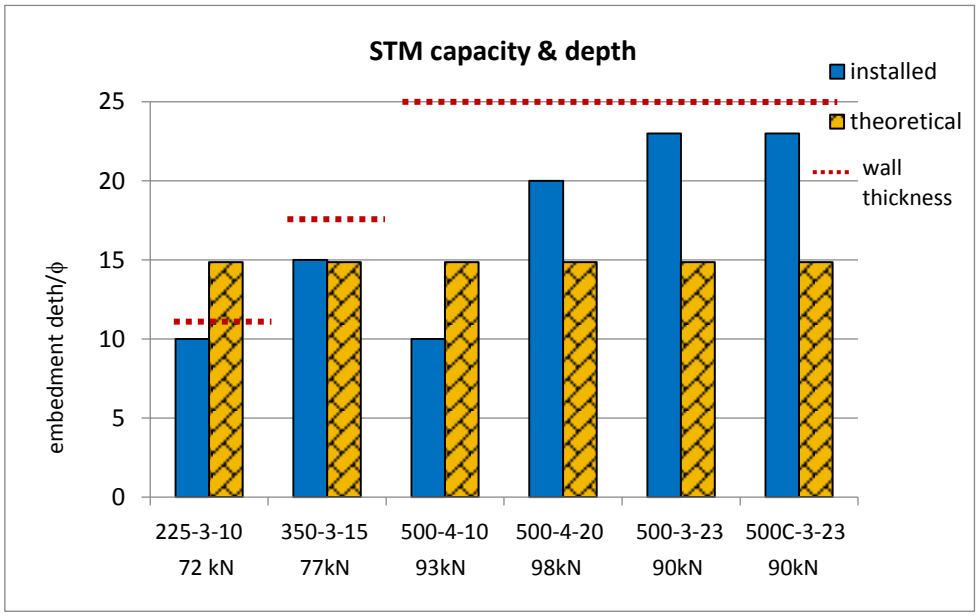

Fig. 8. Theoretical peak load and corresponding embedment depth at strut angle 60^{o}

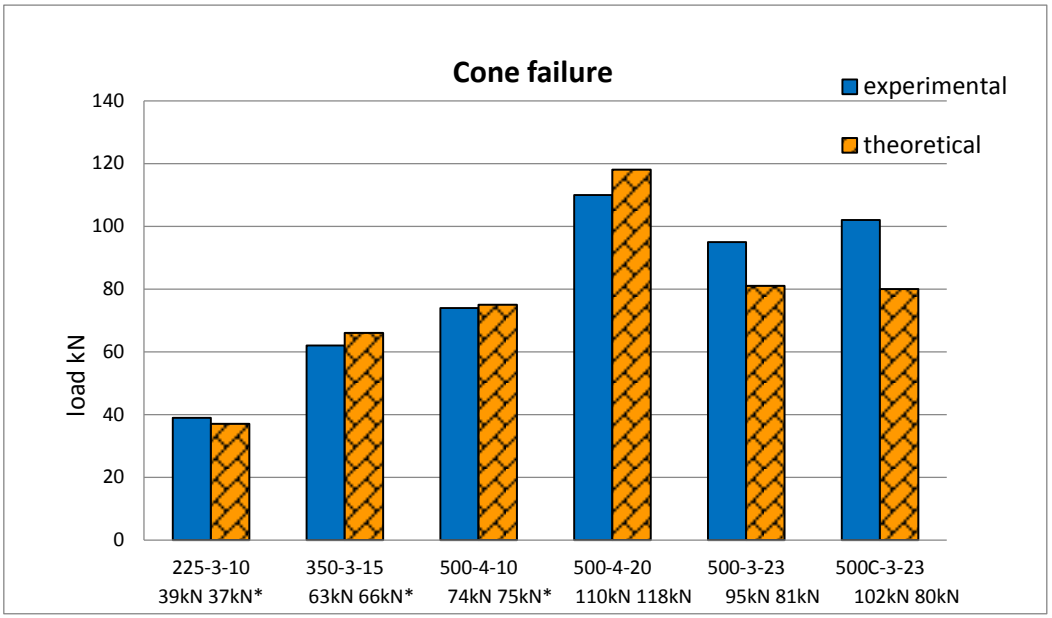

Fig. 9. Experimental and theoretical load for cone failure (* use of Ψ_M)

Appendix A – Experimental Plates

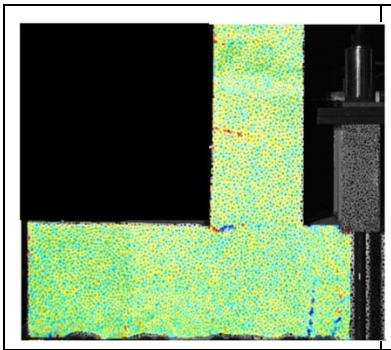	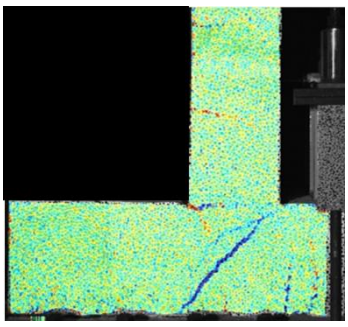	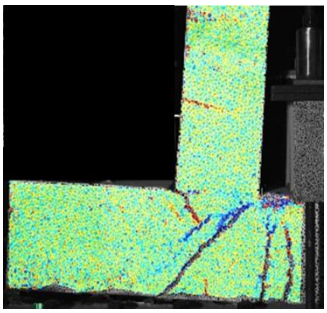
Bottom bending crack at 27 kN	1st primary crack at 39 kN – Y^F & C mode	Peak at 45 kN - Y^F & B mode Wall damaged

Plate: 250-3-10 (BA design method control)

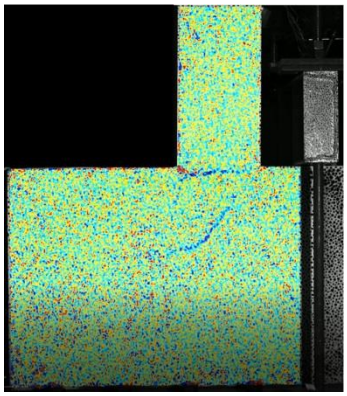	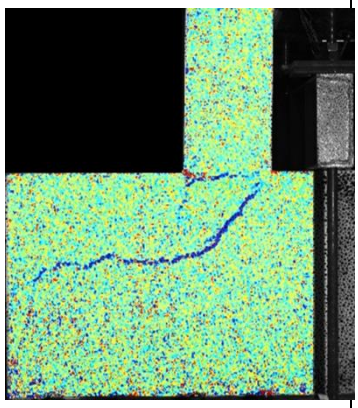	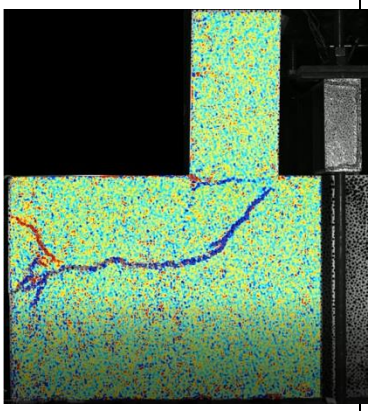
1st primary crack at 59 kN – forming of C mode	Horiz. cracking at 74 kN - C mode	Wall damaged at 84 kN due to strengthen by edge reinforcement

Plate: 500-4-10 (BA design method control)

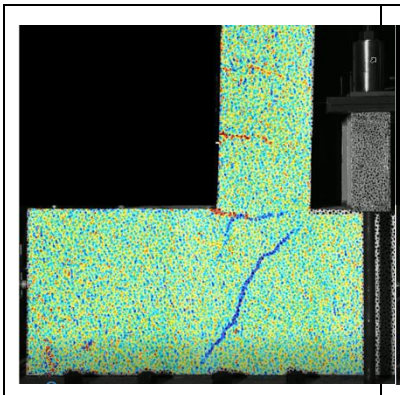	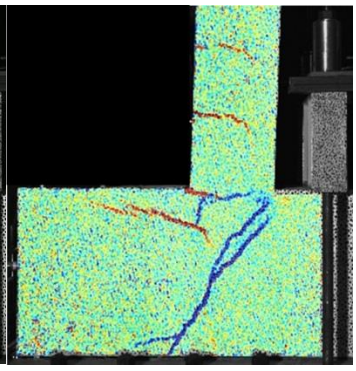	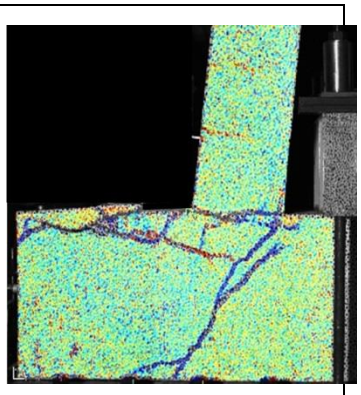
1st primary crack at 63 kN - C mode	At 70 kN - Y mode 2nd primary crack at 77 kN - S mode	Peak at 80 kN - C mode Wall damaged

Plate: 350-3-15 (BA design method control)

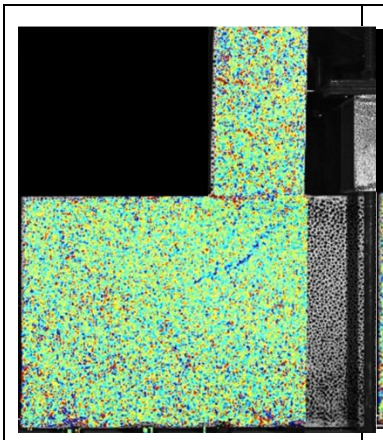	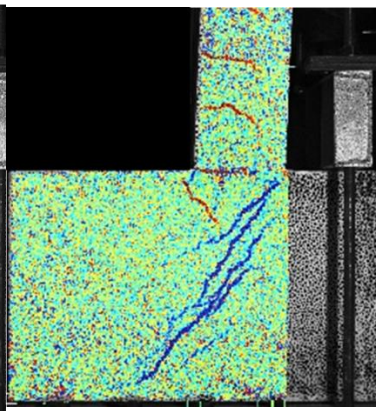	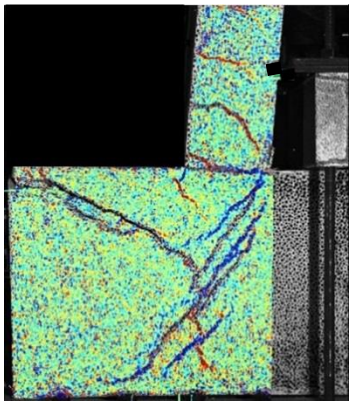
1st primary crack at 93 kN - S mode	At 98 kN - Y mode 2nd primary crack at 110 kN – C mode	Peak at 127 kN – Y^N,S & H mode Slab & wall damaged

Plate: 500-4-20 (STM control)

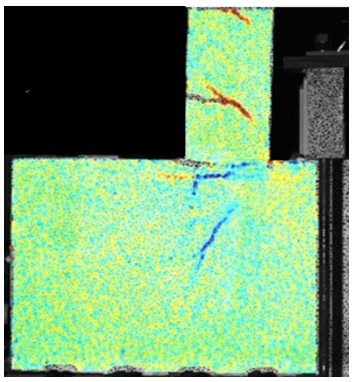	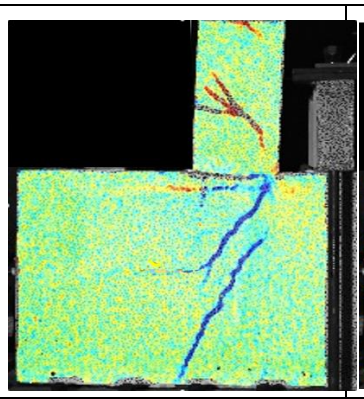	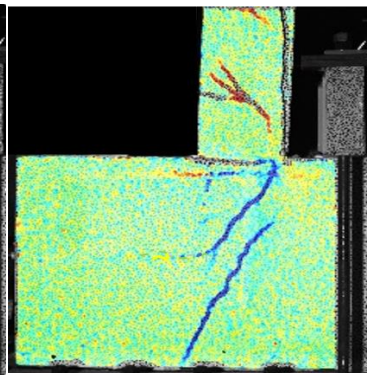
At 83 kN - PIR Y mode 1st primary crack at 91 kN - S mode	2nd primary crack at 95 kN – C mode	Peak at 100 kN – S mode Slab & wall damaged

Plate: 500-3-23 (STM control)

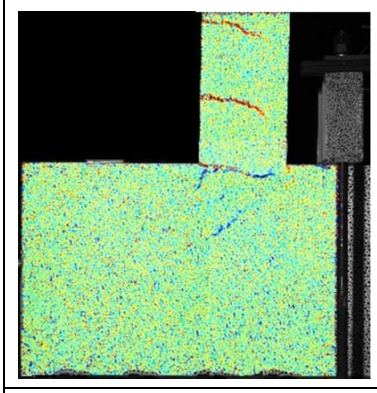	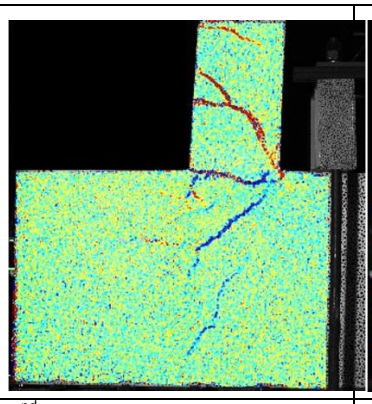	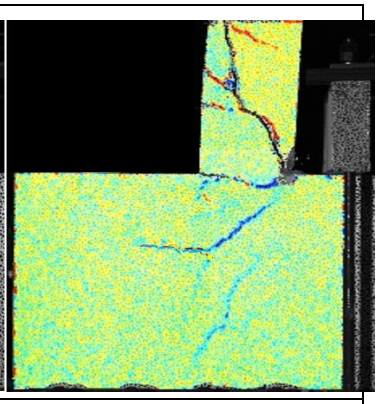
At 78 kN - PIR Y mode 1st primary crack at 89 kN - S^L mode	2nd primary crack at 102 kN – C mode	Peak at 102 kN – S mode Slab & wall damaged

Plate: 500C-3-23 (STM control)

Note: failure mode for Y – PIR yield; Y^N –NF reinf. yield; Y^F – FF reinf. yield; C – cone; H – shear; S – strut; B – combined cone and bond failure

Appendix B – Theoretical Calculation Example

Sample C500-4-20 is a good example to demonstrate the theoretical calculation because there are various failure modes found before reaching the peak load of 127 kN. The first and secondary primary cracks form at a load of 93 kN and 110 kN, respectively. The PIR yield at 98 kN. The strut inclination angle is found to be 50^o in the experiments.

PIR strength

For a closing moment case, take $z_{1r} = 130$

$F_{s10} = M_1 / z_{1r} = V \, x \, 885/130 = 6.8 \, V$; $A_{s1} = 4 \, x \, \pi \, x \, 20^2/4 = 1257$

$\sigma_{s1} = 6.8 \, V \, x 10^3/1257 < 540 MPa$

Hence, V = 100 kN if PIR start to yield. At 115 kN will be the ultimate yield. No force greater than this can be exerted on the wall structure through the PIR system.

R = 98/100 = 0.98; Y – mode failure

$R = 127/115 = 1.10$; Y^u – mode failure

Anchorage length

Reinforcement perimeter $\Sigma u = 4 \cdot \pi \cdot 20 = 251$ mm

$F_{s10} = 115 \, x \, 885/130 = 781$ (ultimate steel force)

$l_b = F_{s10} / (f_{bm} \cdot \Sigma u) = 781 \, x \, 10^3/(21.6 \, x \, 251) = 144$

$z_0 = z_{1r} \cdot tan \, \theta = 130 \, tan \, 50^o = 155$

$l_m = c_s + l_b /2 + z_0 = 45 + 144/2 + 155 = 272 < l_{b\,n} = 400$ mm installed

Similarly, for $V_1 = 96$ kN as shown in the following table:

PIR	V_1	F_{s10}	l_b	l_m
yield	100	681	125	263
Ultimate yield	≥ 115	781	144	272

Wall FF reinforcements (bending check):

$F_{s3} = M_1/z_3 = V \, x \, 885/410 = 2.16 \, V$

$\sigma_{s3} = F_{s3}/A_{s3} = 2.16 \, V \, x \, 1000/1257 < 540$

Hence, V = 314 kN

$R = V_{exp}/V_{theo} = 127/314 = 0.40$; FF reinforcements do not yield

Wall NF reinforcements:

$F_{s0} = M_1 \cdot (1/z_0 - 1/z_2) = V \times 885 \times (1/155 - 1/410) = 3.43\ V$

$\sigma_{s0} = F_{s0}/A_{s0} = 3.43\ V \times 1000/ (4 \times \pi \times 16^2/4) < 540.$

Hence, V = 127 kN

$V_{exp}/V_{theo} = 127/127 = 1.0$; Y^N – mode failure

Compressive strut

For validating first primary crack (Crack 1), applied force of 96 kN is applied:

$\eta_{fc} = (30/f_c)^{1/3} = (30/(0.8 \times 35.3)^{1/3} = 1.02 \leq 1.0$

$\alpha = 0.75 \times 1.0 = 0.75$

$D_R = \alpha \cdot f_c \cdot (b \cdot l_b \cdot cos\ \theta) = 0.75 \times 0.8 \times 35.3 \times (500 \times 125 \times cos\ 50^o)/1000 = 853$ kN

$F_{c0} = M_1 / z_0 = 96 \times 885/155 = 548$

$D_0 = F_{c0} / cos\ \theta = 548 / cos\ 50^o = 853\ kN \leq D_R$

Hence, compressive strut failure takes place at applied force of 96 kN.

R = 93/96 = 0.97 ; S – mode occurs when PIR yield

For validating peak with steel reaching ultimate strength, 115 kN rather than peak load of 127 kN is used:

$D_R = \alpha \cdot f_c \cdot (b \cdot l_b \cdot cos\ \theta) = 0.75 \times 0.8 \times 35.3 \times (500 \times 144 \times cos\ 50^o)/1000 = 981$ kN

$F_{c0} = M_1 / z_0 = 127 \times 885/ 155 = 725$ kN

$D_0 = F_{c0} / cos\ \theta = 1129 > D_R$

R = 1127/981 = 1.14 kN ; S – mode occurs when reaching PIR ultimate strength

Splitting strength

$F_{c0} = M_1 / z_0 = 127 \times 885/155 = 725$

$M_{sp} = F_{c0} \cdot z_0 \cdot (1 – z_0/z) \cdot (1 - l_b /2z) = 725 \times 155 \times (1 - 155/410) (1 - 144/2 \times 410) \times 10^{-3} = 57.6$

$W_{sp} = b \cdot z^2 /2.41 = 500 \times 410^2/2.41 \times 10^{-6} = 34.9$

$\sigma_{sp} = M_{sp} / W_{sp} = 1.65$

$R = \sigma_{sp}/f_{ct} = 1.65/2.49 = 0.66$; No splitting failure.

Cone failure

From the experiments, the anchorage strength of the PIR is found dependent on both embedment depth l_{bn} (= 400) and the number of PIR bars. Hence, take effective depth h_{ef} as the bar spacing,

h_{ef} = s = (500 – 2(82.5))/3 = 111.7

$c_{cr,N} = 1.5 \cdot h_{ef} = 1.5 \, x \, 111.7 = 167.6$ and $s_{cr,N} = 3 \cdot h_{ef} = 335$

$\Psi_{s,N} = 0.7 + 0.3 \, c/c_{cr,N} = 0.7 + 0.3 \, x \, 82.5/167.6 = 0.85$

$\Psi_M = 2.5 - z_1/ h_{ef} = 2.5 - 130/400 = 2.18 > 2.0$ (from Eq. (12b))

With other coefficients = 1.0 and mean values are considered rather than characteristic values, from Eq. (11)

Half cone capacity at the PIR tip, strut effect (θ =72°) due to Ψ_M becomes ineffective:

$N_{R,C} = 10.1/0.75 \cdot f'^{0.5}_c \cdot l_{bn}^{1.5} \cdot A_{c,N} / A^0_{c,N} \cdot \Psi_{S,N}$

$= 10.1/0.75 \, x \, 35.3^{0.5} \, x \, 400^{1.5} \, x \, 500 \, /335 \, x \, 0.85/1000 = 810$ kN

$N_C = 110 \, x \, 885/130 = 750$ kN

R = 750/810 = 0.93 ; C – mode failure

As within 0.9 < R < 1.0, half cone failure might happen at V_1 = 110 kN

Full cone capacity in PIR including strut effect due to Ψ_M:

$N_{R,C} = 10.1/0.75 \cdot f'^{0.5}_c \cdot l_{bn}^{1.5} \cdot A_{c,N} / A^0_{c,N} \cdot \Psi_{S,N} \cdot \Psi_M$

$= 10.1/0.75 \, x \, 35.3^{0.5} \, x \, 400^{1.5} \, x \, 500 \, /335 \, x \, 0.85 \, x \, 2 \, /1000 = 1620$ kN

R = 781/1620 = 0.48 kN ; No full cone failure.

<u>Combined cone and bond capacity:</u>

$S_{cr,Np} = 7.3 \, \phi \cdot (\tau_{Rk} /0.75)^{0.5} \leq 3 \, h_{ef} = 3 \, x \, 111.7 = 335$

$C_{cr,Np} = 335/2 = 167.5$

$\Psi_{s,N} = 0.7 + 0.3 \, c/c_{cr,N} = 0.7 + 0.3 \, x \, 82.5/167.5 = 0.85$

$\Psi_M = 2.5 - z_1/ l_{bn} = 2.5 - 130/400 = 2.18 > 2.0$

As the other coefficients are equal to 1.0, Eq. (14) is simplified to:

$N_{Rp} = \pi \cdot \phi \cdot l_{bn} \cdot f_{bm} \cdot A_{p,N} /A^0_{p,N} \cdot \Psi_{s,Np} \cdot \Psi_M$

$= \pi \, x \, 20 \, x \, 400 \, x \, 21.6 \, x \, 500/335 \, x \, 0.85 \, x \, 2/1000 = 1377$ kN

Combined cone and bond failure does not take place.